

New Constraints on the Supranuclear Equation of State and the Hubble Constant from Nuclear Physics – Multi-Messenger Astronomy

Tim Dietrich^{1,2}, Michael W. Coughlin³, Peter T. H. Pang^{2,4}, Mattia Bulla⁵, Jack Heinzel^{6,7}, Lina Issa^{5,8}, Ingo Tews⁹, and Sarah Antier¹⁰

¹ *Institut für Physik und Astronomie, Universität Potsdam,*

Haus 28, Karl-Liebknecht-Str. 24/25, 14476, Potsdam, Germany

² *Nikhef, Science Park 105, 1098 XG Amsterdam, The Netherlands*

³ *School of Physics and Astronomy, University of Minnesota, Minneapolis, Minnesota 55455, USA*

⁴ *Department of Physics, Utrecht University, Princetonplein 1, 3584 CC Utrecht, The Netherlands*

⁵ *Nordita, KTH Royal Institute of Technology and Stockholm University,*

Roslagstullsbacken 23, SE-106 91 Stockholm, Sweden

⁶ *Carleton College, Northfield, MN 55057, USA*

⁷ *Artemis, Université Côte d'Azur, Observatoire Côte d'Azur,*

CNRS, CS 34229, F-06304 Nice Cedex 4, France

⁸ *Université Paris-Saclay, ENS Paris-Saclay, Département de Physique, 91190, Gif-sur-Yvette, France*

⁹ *Theoretical Division, Los Alamos National Laboratory, Los Alamos, NM 87545, USA and*

¹⁰ *APC, UMR 7164, 10 rue Alice Domon et Léonie Duquet, 75205 Paris, France*

(Dated:)

Neutron-star mergers are associated with violent phenomena that probe physical principles under extreme conditions that are not reproducible in any terrestrial laboratory. Thus, their multi-messenger analysis combining gravitational-wave and electromagnetic signatures from multiple wavelengths is not only of astrophysical interest, but it also allows studying the behavior of supranuclear dense matter, testing the fabric of spacetime, probing the principles of general relativity, and measuring the expansion rate of the Universe. In this work, we perform a multi-messenger analysis of the gravitational wave signal GW170817 and its electromagnetic counterparts AT2017gfo and GRB170817A. By incorporating information from the NICER observation of PSR J0030+0451, the radio observations of PSR J0740+6620, and nuclear theory computations using chiral effective field theory, we provide new constraints on the neutron-star equation of state and the Hubble constant. For our analysis, we make also use of the new waveform approximant IMRPhenomPv2_NRTidalv2 for the interpretation of the gravitational wave signal, we employ a newly developed kilonova model, and we derive a new prediction for the debris disk mass surrounding the binary neutron star merger remnant. We determine the radius of a 1.4 solar mass neutron star to be $R_{1.4M_{\odot}} = 10.98_{-0.38}^{+0.37}$ km at 1σ uncertainty and $R_{1.4M_{\odot}} = 10.98_{-0.69}^{+1.00}$ km at 2σ uncertainty. In addition, we estimate the Hubble constant to be $H_0 = 68.4_{-4.7}^{+5.2}$ km/Mpc/s at 1σ uncertainty. We test the consistency of our results and the robustness of our methods by also analyzing the second binary neutron-star merger detection GW190425 and the fact that no electromagnetic counterpart was observed for this event.

Introduction: Recent progress in the field of multi-messenger astronomy allows to address some of the most fundamental questions of current astrophysics research. The multi-messenger observation of binary neutron-star (BNS) mergers allows to elucidate properties of matter under extreme conditions, by unraveling the internal structure of neutron stars, and to determine the expansion rate of the Universe. So far, the most prominent multi-messenger observation was the joined detection of gravitational waves (GWs), GW170817 [1], a gamma ray burst (GRB), GRB170817A, a non-thermal GRB afterglow [2], and a thermal kilonova in the optical and near-optical bands, AT2017gfo [3], from the same astrophysical source. This event enabled already a new, independent measurement of the Hubble constant via GWs [4–6] and the observed kilonova [7, 8] and it allowed to place new constraints on the equation of state of cold matter at supranuclear densities, e.g., [1, 9–17]. While for the second GW observation of a BNS system, GW190425 [18], no electromagnetic (EM) counterpart was observed [19], the event increased the evidence

that BNS systems will be regularly detected. Moreover, GW190425 and GW170817 have different properties and distances what shows the great diversity of BNS events found by GWs. Very recently, also the dedicated observations of PSR J0030+0451 by the Neutron Star Interior Composition Explorer (NICER) [20, 21] improved our understanding of neutron-star interiors and their surrounding spacetime.

In this article, we present a new nuclear physics – multi-messenger astronomy framework by combining knowledge from GW170817, AT2017gfo, GRB170817A, GW190425, PSR J0030+0451, and PSR J0740+6620 with nuclear-theory calculations of the equation of state using chiral effective field theory (EFT) predictions at low densities. In contrast to previous studies, in which the GW analysis has been connected to nuclear-physics predictions, e.g., [9, 14, 17], and to Bayesian analyses of EM and GW signals, e.g., [15, 16, 22], our study is the first to combine all approaches to allow a proper modelling of the kilonova signature of AT2017gfo incorporating constraints from nuclear physics theory. Thus,

we present the first multi-messenger – nuclear physics constraints that explain the observational lightcurves and spectra and also give an updated Hubble constant measurement. All analysis steps benefit from various improvements with respect to previous works, e.g., a new waveform model is employed to analyse the GW signals GW170817 and GW190425 [23], new and improved kilonova models are used to analyse the kilonova AT2017gfo [24], and upgraded phenomenological relations derived from a large set of full 3+1-dimensional numerical relativity simulations are employed to link the kilonova observation to source properties.

Multi-Messenger Analysis: We use a multi-step procedure, as outlined in Fig. 1, to incorporate known constraints from nuclear theory and different multi-messenger observations, i.e., we try to fill the gap of approximative knowledge from a single point of view analysis by combining different observables. Detailed descriptions about the methods used in each step are provided in the supplementary material.

Our analysis of the observational data starts from a large set of 5000 cold equations of state that describe the structure of neutron stars. At low densities, these equations of state are constrained by microscopic calculations using chiral effective-field theory (EFT) interactions and advanced many-body methods. Chiral EFT is a systematic theory for nuclear forces that describes the interactions in terms of nucleon and pion degrees of freedom and includes all interaction mechanisms consistent with the symmetries of Quantum Chromodynamics, the fundamental theory for strong interactions [25–29]. The resulting forces are expanded in powers of momenta, resulting in an order-by-order expansion for nuclear interactions, which is then truncated at a given level. This systematic scheme allows to estimate theoretical uncertainties from missing higher-order contributions to the nuclear interactions. The resulting nuclear Hamiltonian is then inserted into the Schrödinger equation which is solved using quantum Monte Carlo methods [30]. The radius of convergence of this expansion is limited to momenta below approximately 600 MeV [31]. Beyond this so-called breakdown scale, chiral EFT interactions and their uncertainty estimates are not reliable anymore. While recent analyses suggest that chiral EFT might be valid up to twice the nuclear saturation density [32], $n_{\text{sat}} = 0.16 \text{ fm}^{-3}$, we adopt a more conservative limit and constrain our equations of state with chiral EFT calculations up to densities of $1.5 n_{\text{sat}}$. At densities above $1.5 n_{\text{sat}}$, we employ a model-agnostic parametric expansion scheme that represents the equation of state in the speed of sound plane [17, 33, 34] and by design respects causality, i.e., the speed of sound is smaller than the speed of light. In addition, all equations of state support neutron stars with at least $1.9 M_{\odot}$ [35]. The resulting set of equations of state is shown in the top row of Fig. 1.

In the next step (second row of Fig. 1), we discard all equations of state which are not in agreement with the 2σ mass-radius measurement of NICER [20], esti-

ated with the three oval spot pulse waveform model (blue shaded region). As visible by comparing with the 2σ contour (orange shaded region) of the two oval spot pulse waveform model, systematic uncertainties are under control; similar constraints arise from the analysis of [21]. Furthermore, we enforce a maximum neutron-star mass within $[1.96 M_{\odot}, 2.32 M_{\odot}]$ (green shaded region). The lower bound on the maximum neutron-star mass is the 2σ bound of the radio observations of PSR J0740+6620 [36], while the upper bound is motivated by the consideration that the final merger remnant of GW170817 was a black hole [11, 37, 38] and corresponds to the maximum mass stated in [37]. The restricted set of equations of state is colored green in the second row of Fig. 1. By sampling over the obtained set of equations of state, we incorporate our previously derived constraints to analyse the GW events GW170817 and GW190425 [39]. The internal structure of the neutron star is inferred from GW signals due to the measurement of tidal effects, which are larger for neutron stars with smaller masses and larger radii. Due to the high total mass of GW190425, which generally suppresses tidal effects, we focus on GW170817, but the analysis of GW190425, the only other confirmed BNS GW detection to date, is included for completeness and as a cross-check for the outlined procedure. By using the parallel *bilby* framework [40], we can employ high-performance computing clusters so that final results are available within a few hours. We use the new waveform model *IMRPhenomPv2_NRTidalv2* [23] for cross-correlation with the observed data and to infer the binary properties from the measured signal. This model is an upgrade of the waveform approximant *IMRPhenomPv2_NRTidal* which has been used as the standard model in the analyses of GW170817 [41] and GW190425 [18].

Next, we analyze the equations of state with respect to AT2017gfo. Our EM analysis is based on an upgraded lightcurve model [24]. To draw conclusions about generic sources, we use the approach outlined in [15], i.e., a Gaussian-Process-Regression framework to compute generic lightcurves for various ejecta-mass properties. To connect the individual ejecta parameters to the properties of the system, we assume that the total ejecta mass, inferred from the analysis of the lightcurves, is a sum of multiple components: dynamical ejecta $M_{\text{ej}}^{\text{dyn}}$ and disk wind ejecta ζM_{disk} : $m_{\text{ej}} = M_{\text{ej}}^{\text{dyn}} + \zeta M_{\text{disk}} + \alpha$. The parameters α , corresponding to a potentially unmodelled component of the total ejecta, and ζ , determining how much mass of the disk is ejected, are unknown and used as free parameters during our analysis. While our interpretation of the dynamical ejecta is based on previous work [22], we employ a new model for the disk wind ejecta component. This improved model is motivated by recent results outlining shortcomings of previous studies for systems with high mass ratios [44]. To overcome this issue, we include explicitly a mass-ratio dependence in the disk mass prediction. This upgrade reduces the uncertainty of the numerical relativity prediction and increases the

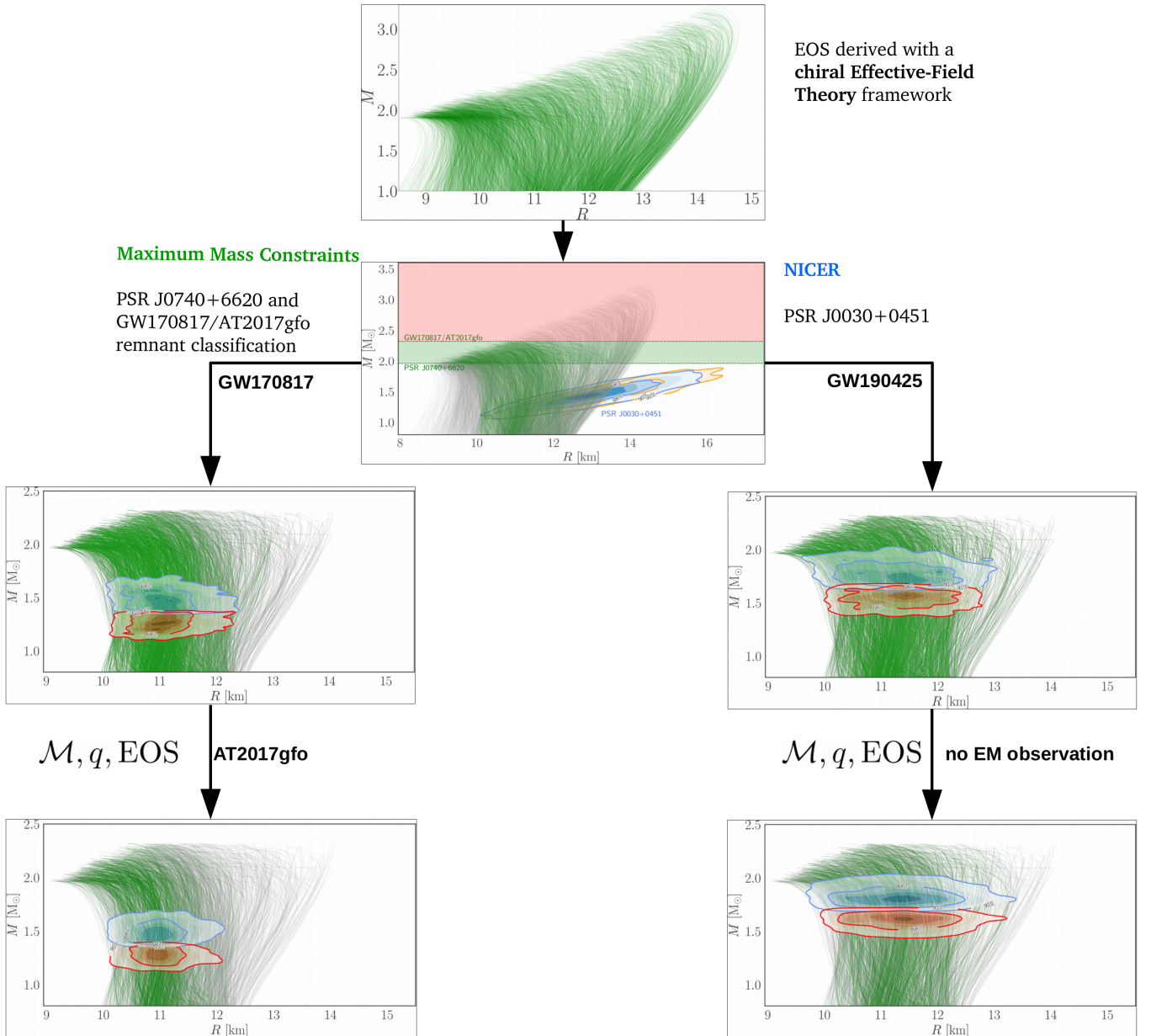


FIG. 1. Multi-step procedure to constrain the supranuclear EOS. We use a set of EOSs constrained by chiral EFT (top panel). This set of EOSs is restricted (only green EOSs remain valid) by incorporating information from the NICER observation of PSRJ0030+0451, the mass measurement of PSRJ0740+6620, and the remnant classification of GW170817/AT2017gfo (ruling out maximum masses in the red shaded region). This restricted set of EOSs is used to reanalyse GW170817 and GW190425, where we show in the third row the 1σ and 2σ contours for the primary star (blue) and the secondary star (red). Finally, we use the obtained results for the chirp mass, the mass ratio, and the EOS as a prior input to analyse AT2017gfo and to obtain our final multi-messenger constraints. For GW190425, we incorporate the fact that no-EM signal was observed but find that this additional information does not add further information beyond the GW analysis.

accuracy of our predictions significantly. To make use of the multi-messenger nature of our analysis, we use the GW results as an input for the analysis of AT2017gfo, i.e., the chirp mass, the mass ratio, and the EOS determine the prior for our EM study.

Following this procedure, we obtain the radius of a $1.4M_{\odot}$ neutron star of $R_{1.4M_{\odot}} = 10.98^{+0.37}_{-0.38}$ km at

1σ uncertainty and $R_{1.4M_{\odot}} = 10.98^{+1.00}_{-0.69}$ km with a 2σ uncertainty (Fig. 1 bottom row). Similarly, for GW190425, we include the fact that no compelling EM counterpart has been observed [19], but this additional information does not add extra constraints beyond the GW data (bottom right panel). Our analysis has the advantage that it explains simultaneously GW170817,

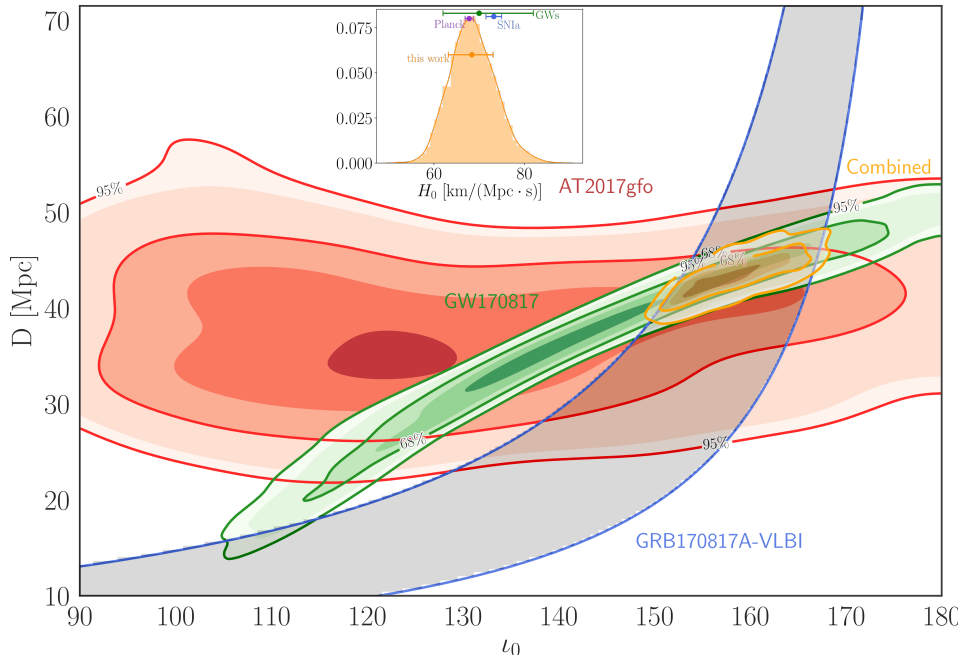


FIG. 2. Estimated distance and inclination from the GW170817 (green) and AT2017gfo analysis (red) together with the VLBI constraint from [5] derived from GRB170817A (blue/gray region). The combined distance-inclination measurement is shown in orange. The inset shows the estimate of the Hubble constant from our combined inclination measurement (orange), we also mark the 1σ results of our study (orange), the Planck measurement [42] (purple), the H_0 measurement related to the distance ladder [43] (blue), and the H_0 -estimate from GW170817 as in [4] (green).

AT2017gfo, GRB170817A, GW190425, the NICER observation of PSR J0030+0451, the radio observations of PSR J0740+6620, but on the other hand is still general and conservative as it allows for strong phase transitions and only employs robust 2σ bounds when observational constraints are incorporated.

Our multi-messenger interpretation of GW170817 and AT2017gfo does not only provide insights into the composition of the neutron-star interior, it also provides an independent measurement of the Hubble constant if we assume that measurable properties related to the time-scale and color evolution of the ejecta are connected to the intrinsic luminosity of the kilonova. References [7, 45] recently showed that models could be used to standardize kilonovae lightcurves and thereby measure their distances. Combining this measurement with the redshift of the host, constraints on the Hubble constant are possible [4]. For this purpose, we can combine the distance and inclination measurement of the GW (green contour in Fig. 2) and kilonova analysis (red contour in Fig. 2). We find that the particular constraint arising from the kilonova observation is not very tight, which is caused by the increased complexity of our lightcurve model compared to previous works. In the supplementary material, we show the consistency with two other kilonova models and proof that our constraints are conservative. In addition, we include the inclination-distance measurement of the Very Long Baseline Interferome-

try presented in Ref. [5]. Ref. [5] found that within 2σ credible interval, the afterglow of GRB170817A can be explained if the inclination and source distance follows $0.25 < \theta \cdot (D/41\text{Mpc}) < 0.5$, see Fig. 2. Combining all measurements leads to an improved distance measurement, which can be related to an estimate of the Hubble constant of $H_0 = 68.4^{+5.2}_{-4.7}$ km/Mpc/s and $H_0 = 68.4^{+9.9}_{-9.4}$ km/Mpc/s at 1σ and 2σ uncertainty, respectively; see orange dataset in the inset of Fig. 2. Unfortunately, based on only one event, the final uncertainty is too large to solve the tension between measurements of Type Ia supernovae via the local distance ladder [43] (blue dataset in the inset of Fig. 2) and the Cosmic Microwave Background [42] (purple dataset in the inset of Fig. 2). However, since our analysis shows only minor systematic errors, we expect that with an increasing number of detections of multi-messenger signals, the measurement uncertainty will decrease as the square-root of the number of detections in the ideal scenario, cf. [4]. Therefore, our derived framework will be used to finally solve the existing Hubble tension.

ACKNOWLEDGMENTS

We thank Kenta Hotokezaka for providing the posterior samples of [5] and Zoheyr Doctor for helpful comments on the manuscript. TD acknowledges support by the European Union's Horizon 2020 research and inno-

vation program under grant agreement No 749145, BNS-mergers. PTHP is supported by the research program of the Netherlands Organization for Scientific Research (NWO). I.T. is supported by the U.S. Department of Energy, Office of Science, Office of Nuclear Physics, under contract No. DE-AC52-06NA25396, by the LDRD program at LANL, and by the NUCLEI SciDAC program. SA is supported by the CNES Postdoctoral Fellowship at Laboratoire Astroparticule et Cosmologie. Computations have been performed on the Minerva HPC cluster of

the Max-Planck-Institute for Gravitational Physics and on SuperMUC-NG (LRZ) under project number pn56zo. Computational resources have also been provided by the Los Alamos National Laboratory Institutional Computing Program, which is supported by the U.S. Department of Energy National Nuclear Security Administration under Contract No. 89233218CNA000001, and by the National Energy Research Scientific Computing Center (NERSC), which is supported by the U.S. Department of Energy, Office of Science, under contract No. DE-AC02-05CH11231.

-
- [1] B. P. Abbott *et al.* (Virgo, LIGO Scientific), *Phys. Rev. Lett.* **119**, 161101 (2017), arXiv:1710.05832 [gr-qc].
- [2] B. P. Abbott *et al.* (Virgo, Fermi-GBM, INTEGRAL, LIGO Scientific), *Astrophys. J.* **848**, L13 (2017), arXiv:1710.05834 [astro-ph.HE].
- [3] *Astrophys. J.* **848**, L12 (2017), arXiv:1710.05833 [astro-ph.HE].
- [4] B. P. Abbott *et al.* (LIGO Scientific, VINROUGE, Las Cumbres Observatory, DLT40, Virgo, 1M2H, MASTER), *Nature*, 10.1038/nature24471 (2017), arXiv:1710.05835 [astro-ph.CO].
- [5] K. Hotokezaka, E. Nakar, O. Gottlieb, S. Nissanke, K. Masuda, G. Hallinan, K. P. Mooley, and A. Deller, *Nature Astron.* (2019), 10.1038/s41550-019-0820-1, arXiv:1806.10596 [astro-ph.CO].
- [6] M. Fishbach *et al.* (LIGO Scientific, Virgo), *Astrophys. J.* **871**, L13 (2019), arXiv:1807.05667 [astro-ph.CO].
- [7] M. W. Coughlin, T. Dietrich, J. Heinzl, N. Khetan, S. Antier, N. Christensen, D. A. Coulter, and R. J. Foley, (2019), arXiv:1908.00889 [astro-ph.HE].
- [8] S. Dhawan, M. Bulla, A. Goobar, A. S. Carracedo, and C. N. Setzer, (2019), arXiv:1909.13810 [astro-ph.HE].
- [9] E. Annala, T. Gorda, A. Kurkela, and A. Vuorinen, *Phys. Rev. Lett.* **120**, 172703 (2018), arXiv:1711.02644 [astro-ph.HE].
- [10] A. Bauswein, O. Just, H.-T. Janka, and N. Stergioulas, *Astrophys. J.* **850**, L34 (2017), arXiv:1710.06843 [astro-ph.HE].
- [11] B. Margalit and B. D. Metzger, *Astrophys. J.* **850**, L19 (2017), arXiv:1710.05938 [astro-ph.HE].
- [12] S. De, D. Finstad, J. M. Lattimer, D. A. Brown, E. Berger, and C. M. Biwer, *Phys. Rev. Lett.* **121**, 091102 (2018), arXiv:1804.08583 [astro-ph.HE].
- [13] B. P. Abbott *et al.* (Virgo, LIGO Scientific), *Phys. Rev. Lett.* **121**, 161101 (2018), arXiv:1805.11581 [gr-qc].
- [14] E. R. Most, L. R. Weih, L. Rezzolla, and J. Schaffner-Bielich, *Phys. Rev. Lett.* **120**, 261103 (2018), arXiv:1803.00549 [gr-qc].
- [15] M. W. Coughlin, T. Dietrich, Z. Doctor, D. Kasen, S. Coughlin, A. Jerkstrand, G. Leloudas, O. McBrien, B. D. Metzger, R. O’Shaughnessy, and S. J. Smartt, *Monthly Notices of the Royal Astronomical Society* **480**, 3871 (2018), arXiv:1805.09371.
- [16] D. Radice and L. Dai, *Eur. Phys. J.* **A55**, 50 (2019), arXiv:1810.12917 [astro-ph.HE].
- [17] C. D. Capano, I. Tews, S. M. Brown, B. Margalit, S. De, S. Kumar, D. A. Brown, B. Krishnan, and S. Reddy, (2019), arXiv:1908.10352 [astro-ph.HE].
- [18] B. P. Abbott *et al.* (LIGO Scientific, Virgo), (2020), arXiv:2001.01761 [astro-ph.HE].
- [19] M. W. Coughlin, T. Dietrich, S. Antier, M. Bulla, F. Foucart, K. Hotokezaka, G. Raaijmakers, T. Hinderer, and S. Nissanke, (2019), arXiv:1910.11246 [astro-ph.HE].
- [20] M. C. Miller *et al.*, *Astrophys. J. Lett.* **887**, L24 (2019), arXiv:1912.05705 [astro-ph.HE].
- [21] T. E. Riley *et al.*, *Astrophys. J. Lett.* **887**, L21 (2019), arXiv:1912.05702 [astro-ph.HE].
- [22] M. W. Coughlin, T. Dietrich, B. Margalit, and B. D. Metzger, *Monthly Notices of the Royal Astronomical Society: Letters* **489**, L91 (2019), arXiv:1812.04803.
- [23] T. Dietrich, A. Samajdar, S. Khan, N. K. Johnson-McDaniel, R. Dudi, and W. Tichy, *Phys. Rev.* **D100**, 044003 (2019), arXiv:1905.06011 [gr-qc].
- [24] M. Bulla, *Mon. Not. Roy. Astron. Soc.* **489**, 5037 (2019), arXiv:1906.04205 [astro-ph.HE].
- [25] S. Weinberg, *Phys. Lett.* **B251**, 288 (1990).
- [26] S. Weinberg, *Nucl. Phys.* **B363**, 3 (1991).
- [27] U. van Kolck, *Phys. Rev.* **C49**, 2932 (1994).
- [28] E. Epelbaum, H.-W. Hammer, and U.-G. Meissner, *Rev. Mod. Phys.* **81**, 1773 (2009), arXiv:0811.1338 [nucl-th].
- [29] R. Machleidt and D. R. Entem, *Phys. Rept.* **503**, 1 (2011), arXiv:1105.2919 [nucl-th].
- [30] J. Carlson, S. Gandolfi, F. Pederiva, S. C. Pieper, R. Schiavilla, K. E. Schmidt, and R. B. Wiringa, *Rev. Mod. Phys.* **87**, 1067 (2015).
- [31] J. A. Melendez, S. Wesolowski, and R. J. Furnstahl, *Phys. Rev.* **C96**, 024003 (2017), arXiv:1704.03308 [nucl-th].
- [32] I. Tews, J. Carlson, S. Gandolfi, and S. Reddy, *Astrophys. J.* **860**, 149 (2018), arXiv:1801.01923 [nucl-th].
- [33] I. Tews, J. Margueron, and S. Reddy, *Phys. Rev.* **C98**, 045804 (2018), arXiv:1804.02783 [nucl-th].
- [34] I. Tews, J. Margueron, and S. Reddy, *Eur. Phys. J.* **A55**, 97 (2019), arXiv:1901.09874 [nucl-th].
- [35] J. Antoniadis, P. C. Freire, N. Wex, T. M. Tauris, R. S. Lynch, *et al.*, *Science* **340**, 6131 (2013), arXiv:1304.6875 [astro-ph.HE].
- [36] H. T. Cromartie *et al.*, (2019), 10.1038/s41550-019-0880-2, arXiv:1904.06759 [astro-ph.HE].
- [37] L. Rezzolla, E. R. Most, and L. R. Weih, *Astrophys. J.* **852**, L25 (2018), arXiv:1711.00314 [astro-ph.HE].
- [38] M. Shibata, E. Zhou, K. Kiuchi, and S. Fujibayashi, *Phys. Rev.* **D100**, 023015 (2019), arXiv:1905.03656 [astro-ph.HE].

- [39] The data release in [46, 47] is used.
- [40] R. Smith and G. Ashton, (2019), arXiv:1909.11873 [gr-qc].
- [41] B. P. Abbott *et al.* (LIGO Scientific, Virgo), Phys. Rev. **X9**, 011001 (2019), arXiv:1805.11579 [gr-qc].
- [42] P. A. R. Ade *et al.* (Planck), Astron. Astrophys. **594**, A13 (2016), arXiv:1502.01589 [astro-ph.CO].
- [43] A. G. Riess *et al.*, Astrophys. J. **826**, 56 (2016), arXiv:1604.01424 [astro-ph.CO].
- [44] K. Kiuchi, K. Kyutoku, M. Shibata, and K. Taniguchi, Astrophys. J. **876**, L31 (2019), arXiv:1903.01466 [astro-ph.HE].
- [45] R. Kashyap, G. Raman, and P. Ajith, *ApJL 886 L19 (2019)*, Astrophys. J. **886**, L19 (2019), [Astrophys. J. Lett.886,L19(2019)], arXiv:1908.02168 [astro-ph.SR].
- [46] LIGO Scientific Collaboration and Virgo Collaboration, <https://www.gw-openscience.org/events/GW170817/> (2017).
- [47] LIGO Scientific Collaboration and Virgo Collaboration, https://www.gw-openscience.org/eventapi/html/03_Discovery_Papers/GW190425/v1/ (2020).
- [48] E. Epelbaum, H. Krebs, and U.-G. Meißner, Eur. Phys. J. A **51**, 53 (2015), arXiv:1412.0142 [nucl-th].
- [49] I. Tews, Z. Davoudi, A. Ekström, J. D. Holt, and J. E. Lynn, (2020), arXiv:2001.03334 [nucl-th].
- [50] A. Gezerlis, I. Tews, E. Epelbaum, S. Gandolfi, K. Hebeler, A. Nogga, and A. Schwenk, Phys. Rev. Lett. **111**, 032501 (2013), arXiv:1303.6243 [nucl-th].
- [51] A. Gezerlis, I. Tews, E. Epelbaum, M. Freunek, S. Gandolfi, K. Hebeler, A. Nogga, and A. Schwenk, Phys. Rev. C **90**, 054323 (2014), arXiv:1406.0454 [nucl-th].
- [52] J. E. Lynn, I. Tews, J. Carlson, S. Gandolfi, A. Gezerlis, K. E. Schmidt, and A. Schwenk, Phys. Rev. Lett. **116**, 062501 (2016), arXiv:1509.03470 [nucl-th].
- [53] J. E. Lynn, I. Tews, S. Gandolfi, and A. Lovato, Ann. Rev. Nucl. Part. Sci. **69**, 279 (2019), arXiv:1901.04868 [nucl-th].
- [54] I. Tews, Phys. Rev. **C95**, 015803 (2017), arXiv:1607.06998 [nucl-th].
- [55] S. Bogdanov *et al.*, Astrophys. J. **887**, L26 (2019), arXiv:1912.05707 [astro-ph.HE].
- [56] The samples have been downloaded from <https://zenodo.org/record/3473466#.XiBajeZKiis>.
- [57] G. Ashton *et al.*, Astrophys. J. Suppl. **241**, 27 (2019), arXiv:1811.02042 [astro-ph.IM].
- [58] F. B. Farr, W. M. and L. T., Collaboration Technical Report.
- [59] C. Cahillane *et al.*, Phys. Rev. D **96**, 102001 (2017).
- [60] A. D. Viets, M. Wade, A. L. Urban, S. Kandhasamy, J. Betzwieser, D. A. Brown, J. Burguet-Castell, C. Cahillane, E. Goetz, K. Izumi, S. Karki, J. S. Kissel, G. Mendell, R. L. Savage, X. Siemens, D. Tuyenbayev, and A. J. Weinstein, Classical and Quantum Gravity **35**, 095015 (2018).
- [61] N. J. Cornish and T. B. Littenberg, Classical and Quantum Gravity **32**, 135012 (2015).
- [62] T. B. Littenberg and N. J. Cornish, Phys. Rev. D **91**, 084034 (2015).
- [63] M. Hannam, P. Schmidt, A. Bohé, L. Haegel, S. Husa, F. Ohme, G. Pratten, and M. Pürrer, Phys. Rev. Lett. **113**, 151101 (2014), arXiv:1308.3271 [gr-qc].
- [64] T. Dietrich, S. Bernuzzi, and W. Tichy, Phys. Rev. **D96**, 121501 (2017), arXiv:1706.02969 [gr-qc].
- [65] T. Dietrich *et al.*, Phys. Rev. **D99**, 024029 (2019), arXiv:1804.02235 [gr-qc].
- [66] B. P. Abbott *et al.* (LIGO Scientific, Virgo), (2019), arXiv:1908.01012 [gr-qc].
- [67] B. P. Abbott *et al.* (LIGO Scientific, Virgo), Phys. Rev. **X9**, 031040 (2019), arXiv:1811.12907 [astro-ph.HE].
- [68] B. P. Abbott *et al.* (LIGO Scientific, Virgo), Phys. Rev. Lett. **123**, 011102 (2019), arXiv:1811.00364 [gr-qc].
- [69] D. Kasen, B. Metzger, J. Barnes, E. Quataert, and E. Ramirez-Ruiz, Nature, 10.1038/nature24453 (2017), 10.1038/nature24453, arXiv:1710.05463 [astro-ph.HE].
- [70] J. Barnes, D. Kasen, M.-R. Wu, and G. Martínez-Pinedo, Astrophys. J. **829**, 110 (2016), arXiv:1605.07218 [astro-ph.HE].
- [71] T. Dietrich and M. Ujevic, Class. Quant. Grav. **34**, 105014 (2017), arXiv:1612.03665 [gr-qc].
- [72] A. Perego, D. Radice, and S. Bernuzzi, Astrophys. J. **850**, L37 (2017), arXiv:1711.03982 [astro-ph.HE].
- [73] K. Kawaguchi, M. Shibata, and M. Tanaka, arXiv e-prints, arXiv:1908.05815 (2019), arXiv:1908.05815 [astro-ph.HE].
- [74] The dynamical ejecta used here is essentially a high-velocity portion of the geometry adopted in Ref. [24].
- [75] Z. Doctor, B. Farr, D. E. Holz, and M. Pürrer, Phys. Rev. **D96**, 123011 (2017), arXiv:1706.05408 [astro-ph.HE].
- [76] M. Pürrer, Class. Quant. Grav. **31**, 195010 (2014), arXiv:1402.4146 [gr-qc].
- [77] D. Radice, A. Perego, K. Hotokezaka, S. A. Fromm, S. Bernuzzi, and L. F. Roberts, Astrophys. J. **869**, 130 (2018), arXiv:1809.11161 [astro-ph.HE].
- [78] T. Dietrich, M. Ujevic, W. Tichy, S. Bernuzzi, and B. Brügmann, Phys. Rev. **D95**, 024029 (2017), arXiv:1607.06636 [gr-qc].
- [79] K. Hotokezaka, K. Kyutoku, H. Okawa, M. Shibata, and K. Kiuchi, Phys.Rev. **D83**, 124008 (2011), arXiv:1105.4370 [astro-ph.HE].
- [80] M. Agathos, F. Zappa, S. Bernuzzi, A. Perego, M. Breschi, and D. Radice, (2019), arXiv:1908.05442 [gr-qc].
- [81] G. Hinshaw, J. L. Weiland, R. S. Hill, N. Odegard, D. Larson, C. L. Bennett, J. Dunkley, B. Gold, M. R. Greason, N. Jarosik, E. Komatsu, M. R. Nolta, L. Page, D. N. Spergel, E. Wollack, M. Halpern, A. Kogut, M. Limon, S. S. Meyer, G. S. Tucker, and E. L. Wright, *apjs* **180**, 225 (2009), arXiv:0803.0732 [astro-ph].
- [82] A. C. Crook, J. P. Huchra, N. Martimbeau, K. L. Masters, T. Jarrett, and L. M. Macri, *apj* **655**, 790 (2007), arXiv:astro-ph/0610732 [astro-ph].
- [83] C. M. Springob, C. Magoulas, M. Colless, J. Mould, P. Erdoğdu, D. H. Jones, J. R. Lucey, L. Campbell, and C. J. Fluke, *mnras* **445**, 2677 (2014), arXiv:1409.6161 [astro-ph.CO].
- [84] J. Carrick, S. J. Turnbull, G. Lavaux, and M. J. Hudson, Monthly Notices of the Royal Astronomical Society **450**, 317–332 (2015).
- [85] This choice of selection effect term is rooted to a volumetric prior on redshift [4].
- [86] D. Foreman-Mackey, D. W. Hogg, D. Lang, and J. Goodman, *PASP* **125**, 306 (2013), 1202.3665.

Supplementary materials

MATERIALS AND METHODS

Chiral effective- field theory and the neutron-star equation of state

From a microscopic viewpoint, nuclear interactions are governed by a multitude of processes, e.g., various longer-range meson-exchanges between two or more nucleons or short-range processes that are typically modeled by contact interactions. Given this large number of operator structures for nuclear interactions, a guiding principle which arranges these operators according to their importance is desirable. Nuclear effective field theories (EFT), like chiral EFT [25–29], allow to do that.

Nuclear EFTs start from the most general Lagrangian that is consistent with all symmetries of the fundamental theory of strong interactions, Quantum Chromodynamics, and that describes the various interaction mechanisms. In chiral EFT, this Lagrangian is written in terms of nucleon and pion degrees of freedom, and includes pion-exchange interactions as well as nucleon-contact interactions. The latter absorb short-range effects, e.g., exchanges of heavier mesons, and depend on coupling constants that have to be adjusted to experimental data. Since this Lagrangian contains an infinite number of terms, it is then expanded in powers of momenta p over the so-called breakdown scale Λ_b . In addition to two-nucleon interactions, the chiral EFT expansion naturally includes also many-body forces, where three or more nucleons interact with each other. The result of this approach is a systematic and consistent expansion of two- and many-body nuclear forces, which can be truncated at a given order, allows for nuclear interactions to be systematically improved, and enables theoretical uncertainty estimates due to our incomplete understanding of nuclear interactions, see, e.g., Ref. [48].

As stated above, the determination of unknown coupling constants is performed by fitting the nuclear Hamiltonians order-by-order to experimental data. Usually, two-nucleon interactions are fit to two-nucleon scattering data, while many-body forces are adjusted in few- or many-body systems. However, new fitting protocols and other improvements are explored by the community, e.g., [49].

Chiral interactions allow a meaningful extrapolation of nuclear interactions away from experimentally accessible systems to systems that are difficult or impossible to measure in terrestrial laboratories, e.g., the neutron-rich matter in the core of neutron stars. However, chiral interactions are limited to momenta $p < \Lambda_b \approx 600$ MeV [31]. At larger momenta, chiral interactions are not reliable because short-range (high-energy) physics that was absorbed by the coupling constants becomes important and needs to be explicitly included.

The equations of state used in this work are constrained at low densities by quantum Monte Carlo calculations of neutron matter [30], in particular with the auxiliary field diffusion Monte Carlo approach, using chiral interactions in their local formulation of Refs. [50–52]. These interactions were fit to two-nucleon scattering data, the ^4He ground state energy, and neutron- α scattering phase shifts. A recent review of this approach can be found in Ref. [53]. In the past, we have analyzed the order-by-order convergence of this approach and found that it remains reasonable up to densities of twice the nuclear saturation density [32]. To be more conservative, here we employ these constraints up to densities of $1.5 n_{\text{sat}}$.

These results, together with their uncertainty bands, allow us to constrain the neutron-star equation of state below $1.5 n_{\text{sat}}$. First, we extend the results to matter in β -equilibrium and add a crust [54]. We extend our EOS models to densities beyond $1.5 n_{\text{sat}}$ by employing a model-agnostic parametric expansion scheme that represents the equation of state in the speed of sound plane [17, 33, 34]. In particular, we sample a set of six randomly distributed points $c_s^2(n)$ between $1.5 n_{\text{sat}}$ and $12 n_{\text{sat}}$ and connect them by line segments. We found that neutron-star properties are not very sensitive to the number of line segments when varying it between 5–10. This construction by design respects causality and stability, $0 \leq c_s \leq c$, with the speed of light c . For each sampled EOS, we construct a second EOS that includes a segment with $c_s = 0$ with random onset density and width, to simulate EOS with strong first-order phase transitions.

This speed-of-sound extension does not make any assumptions about degrees of freedom at higher densities, and includes many possible density dependencies for the EOS at high densities. For example, this extension includes regions of sudden stiffening or sudden softening, as would be expected from a strong first-order phase transition. From the speed-of-sound curve, we reconstruct the EOS and solve the Tolman-Oppenheimer-Volkoff equations to extract neutron-star structure properties. In addition, all equations of state are required to support neutron stars with at least 1.9 solar masses [35]. In this work, we have sampled 5000 different EOS that give a uniform prior on the radius of a typical $1.4 M_\odot$ neutron star.

Incorporation of NICER data

For our inclusion of the recent NICER data [55], we use the results presented in [20] where a Bayesian inference approach is used to analyze the energy-dependent thermal X-ray waveform of PSR J0030+0451. Our study employs the publicly available samples obtained with the best-fit approximant of Ref. [20], namely a three oval, uniform-temperature spots model[56]. This model provides excellent agreement with the observed NICER data and allows to infer the mass and radius of PSR J0030+0451 to be $M = 1.44^{+0.15}_{-0.14} M_{\odot}$ and $R = 13.02^{+1.24}_{-1.06}$ km (both at 1σ uncertainty). As pointed out in [20, 21] the inferred mass-radius relations are not dominated by systematic uncertainties and inferred parameters are in good agreement for different models; as a comparison the results for the two oval spot model are also shown in Fig. 1 (orange contours).

As a conservative approach, we use the 2σ errors and discard all EOSs from our set of chiral EFT EOSs which do not overlap with the 2σ region presented in Fig. 1.

GW170817 and GW190425

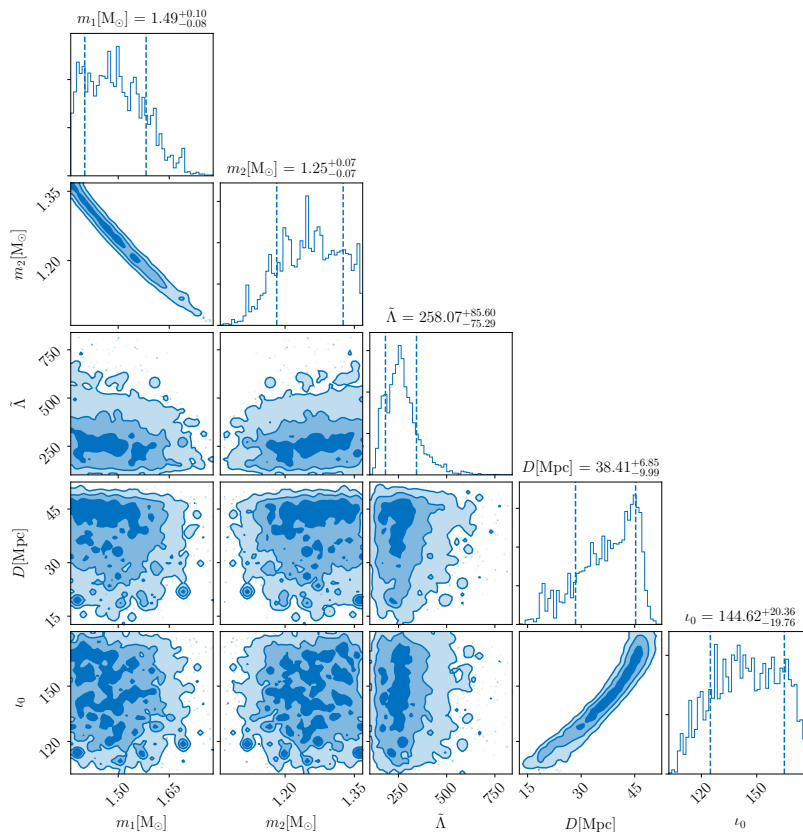


FIG. 3. Corner plot of the inferred GW170817’s parameters which are used for further analysis. The parameters shown are; primary source mass m_1 , secondary source mass m_2 , mass-weighted tidal deformability $\tilde{\Lambda}$, luminosity distance D and inclination i_0 .

We use the `bilby` infrastructure [57] to reanalyze GW170817 and GW190425. With the help of `parallel bilby` [40] we can run on 800 compute cores to obtain final posteriors within a few hours on the HPC clusters Minerva at the Max-Planck-Institute for Gravitational Physics or on SuperMUC-NG at the Leibniz Supercomputing Centre. The GW signals are analysed within a frequency interval of $f \in [23, 2048]$ Hz which covers the full inspiral of the binary neutron stars coalescence. Frequency-dependent spline calibration envelopes [58] are introduced into the waveform templates to counteract the potential systematics due to the uncertainties in the detectors’ calibrations [59, 60]. We also use the power spectral density, which is used by the gravitational-wave data analysis, estimated with BayesWave [61, 62].

We use for the first time the new `IMRPhenomPv2_NRTidalv2` waveform model. The approximant augments the precessing binary black hole waveform [63] with the description outlined in [23]. `IMRPhenomPv2_NRTidalv2` has

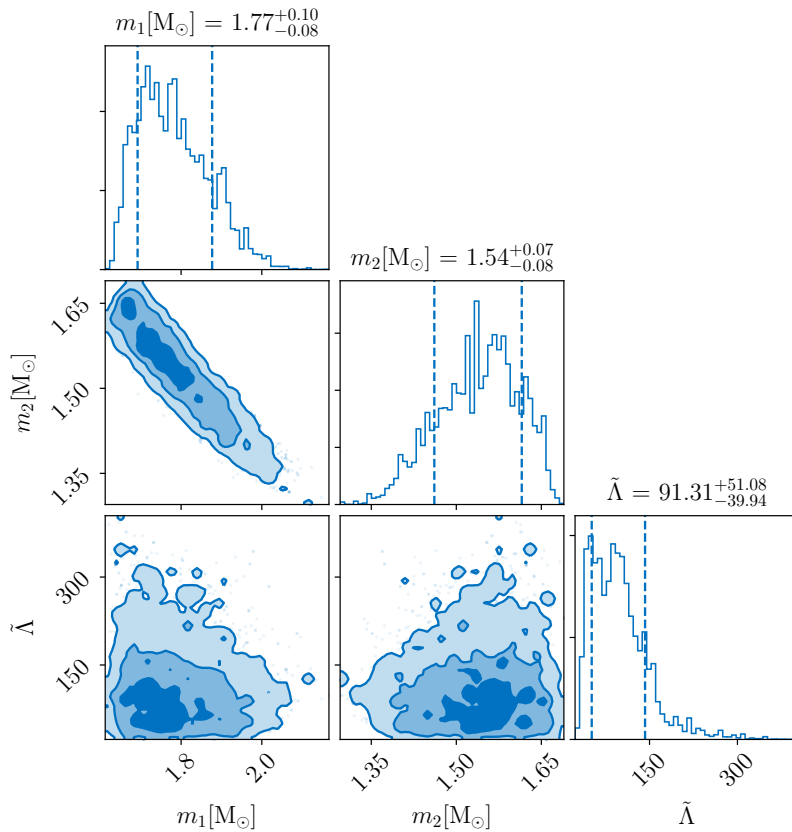


FIG. 4. Corner plot of the inferred GW190425’s parameters which are used for further analysis. The parameters shown are; primary source mass m_1 , secondary source mass m_2 and mass-weighted tidal deformability $\tilde{\Lambda}$.

an improved tidal and spin description compared to the `IMRPhenomPv2_NRTidal` [64, 65] model, which has been the standard waveform employed by the Ligo Scientific and Virgo Collaborations to interpret GW170817 [13, 41, 66–68] and GW190425 [18]. We present the parameter estimation results of the most important parameters for our study in Fig. 3 for GW170817 and in Fig. 4 for GW190425.

AT2017gfo

Kilonova modelling

For the assessment of systematic uncertainties, we compare different lightcurve models mainly based on [24] and [69].

Model I (standard model): Here we use Spectral Energy Distributions (SEDs) simulated using the multi-dimensional Monte Carlo radiative transfer code `POSSIS` [24]. In particular, we present a new modelled grid that differs from the one in Ref. [24] in terms of the underlying physics and the assumed geometry for the ejecta. In terms of physics, there are two main differences compared to simulations presented in Ref. [24]: thermalization efficiencies are taken from Ref. [70] and the temperature is no longer parametrized and uniform throughout the ejecta but rather estimated in each grid cell and at each time from the mean intensity of the radiation field (inferred from the density and local energy deposition from radioactive decay). In terms of the adopted geometry, we run calculations for a geometry (Fig. 5) more similar to the one described in, e.g., Refs. [71–73] and obtained from numerical relativity simulations. A first component represents the dynamical ejecta, extending from $v_{\min}^{\text{dyn}} = 0.08c$ to $v_{\max}^{\text{dyn}} = 0.3c$, characterised by an ejecta mass $m_{\text{ej}}^{\text{dyn}}$ and with lanthanide-rich composition within an angle $\pm\phi$ about the equatorial plane and lanthanide-free composition otherwise [74]. The opacities assumed in the dynamical ejecta have the same wavelength- and time-dependence as in Ref. [24], with $\kappa_{\text{bb}}[1\mu\text{m}, 1.5\text{d}] = 1\text{cm}^2\text{g}^{-1}$ for the lanthanide-rich and $\kappa_{\text{bb}}[1\mu\text{m}, 1.5\text{d}] = 5 \times 10^{-3}\text{cm}^2\text{g}^{-1}$ for the lanthanide-free portion of the ejecta (see Ref. [24] for more details). A second spherical component represents the

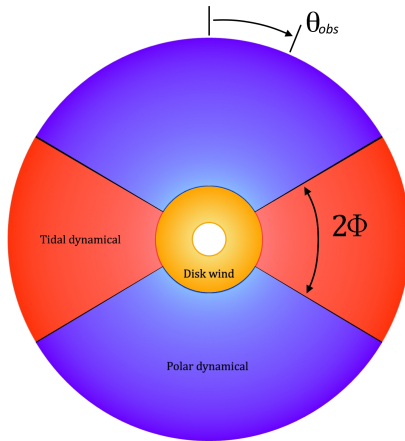


FIG. 5. Geometry employed in our Model I kilonova description, where different colors refer to the different lanthanide fractions of the individual ejecta components.

ejecta released from the merger remnant and debris disk, extending from $v_{\min}^{\text{pm}} = 0.025c$ up to $v_{\max}^{\text{pm}} = 0.08c$ and with an ejecta mass $m_{\text{ej}}^{\text{pm}}$. Opacities adopted for the post-merger ejecta are intermediate [72] to those in the lanthanide-rich and lanthanide-free components of the dynamical ejecta ($\kappa_{\text{bb}}[1\mu\text{m}, 1.5\text{d}] = 0.1\text{ cm}^2\text{ g}^{-1}$). SEDs and corresponding lightcurves are then controlled by four parameters: $m_{\text{ej}}^{\text{dyn}}$, $m_{\text{ej}}^{\text{pm}}$, ϕ and the observer viewing angle θ_{obs} .

Model II: In addition to our updated kilonova model, we also include a version similar to the one in [24], i.e., a model without an additional wind ejecta component. This model has the advantage that a standardization and therefore an extraction of the Hubble constant is easier due to the smaller number of free parameters and that therefore more tighter constraints on the distance and inclination angle are extracted compared to our standard choice (Model I); cf. Fig. 9.

Model III: As an alternative approach and to validate our results, we use the radiative transfer model of Ref. [69]. This model employs a multi-dimensional Monte Carlo code to solve the multi-wavelength radiation transport equation for an expanding medium. We assume one spherical symmetric ejecta component characterized by the mass of the ejecta m_{ej} , the mass fraction of lanthanides X_{lan} , and the ejecta velocity v_{ej} . While using only one ejecta component reduces the consistency between the observational data and the model prediction, it allows an easier standardization and therefore puts a tighter constraint on the measured distance, but no information about inclination can be extracted due to the assumption of spherical symmetry.

Surrogate Construction

In order to draw conclusions about generic sources, we use the approach outlined in Refs. [75, 76], where a Gaussian-Process-Regression framework is employed; cf. Refs. [15, 19] for a detailed discussion. We present the performance of our standard model (Model I) in Fig. 6 and find that it is capable of describing the observed data.

The extracted properties of the ejecta are shown in Fig. 7. We find that the disk wind ejecta is about 10 times larger than the dynamical ejecta, unfortunately, the angle Φ (cf. Fig. 6) is not well constrained, while the observation angle θ peaks around 50° .

To connect the individual ejecta components to the different ejecta mechanisms, we assume that the total ejecta mass is a sum of multiple components. The first component is related to the dynamical ejecta $m_{\text{ej}}^{\text{dyn}}$, i.e., to the material released during the merger process via shocks and torque. The second component is caused by disk wind ejecta and proportional to the disk mass surrounding the final remnant $m_{\text{ej}}^{\text{pm}} = \zeta m_{\text{disk}}$. To allow a conservative estimate, we also add a third component α that we keep as a free parameter during the sampling procedure.

For the dynamical ejecta, we use the description in Ref. [22], while we assume that the disk wind ejecta is proportional to the disk mass. Based on recent works outlining potential issues of previous relations predicting the disk mass for systems with high mass ratios, we have extended previous studies to include an explicit mass-ratio dependence, see discussion below.

The extracted binary properties are shown in Fig. 8, in which we report the chirp mass, the mass ratio, the deformability $\tilde{\Lambda}$, the fraction of the dynamical ejecta α , the disk conversion factor ζ , and the maximum TOV mass. We point out that the tidal deformability and the maximum TOV-mass are just reported as a crosscheck and that the

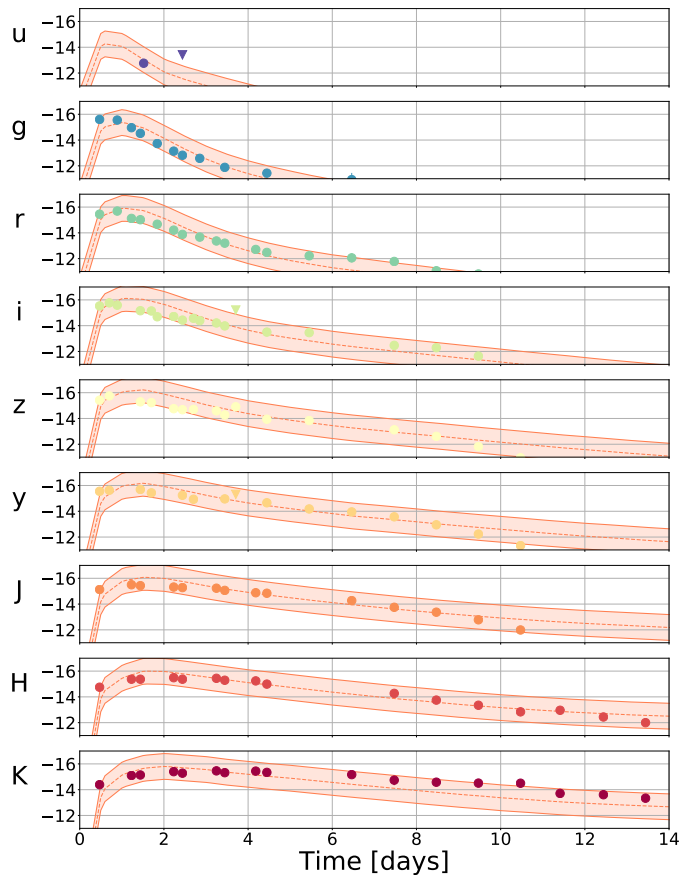


FIG. 6. Observed lightcurves of AT2017gfo in different bands and the predictions of Model I. Observational data are taken from [15].

internal EOS index is used during the Bayesian Inference. Furthermore, we do find very good agreement between the three kilonova models. The biggest difference between all three models is visible in the measurement of the inclination and distance. Therefore, we show the inclination-distance measurement in Fig. 9. Model I is the least constraining due to the fact that the additional wind ejecta component increases the complexity of the model and therefore makes a standardization more complicated, cf. Model II. Model III is spherical symmetric and therefore only allows a distance measurement. In summary, all three models agree within their statistical error measurement, which shows that our analysis is dominated by statistical effects rather than systematics.

New disk mass prediction

We collect a set of results from 73 numerical relativity simulations performed by different groups [44, 77–79]. The full dataset is shown in Fig. 10 (left panel) in which we plot the disk mass versus the ratio of the total mass of the system and the threshold mass. The threshold mass determines when prompt collapse formation after the merger of the two stars happens. For the estimate of the threshold mass, we use the predictions of Ref. [80]. We compare the data with the estimate in Ref. [22] (solid black line) and it becomes evident that, as outlined in Ref. [44], an increasing mass ratio leads to an increased disk mass. To update the fit, we use a similar functional behavior as suggested in Ref. [22], but we incorporate mass-ratio dependent fitting parameters that are obtained by minimizing

$$\log_{10}(M_{\text{disk}}) = \max \left(-3, a \left(1 + b \tanh \left(\frac{c - M/M_{\text{threshold}}}{d} \right) \right) \right), \quad (1)$$

where a, b are

$$\begin{aligned} a &= a_o + \delta a \xi \\ b &= b_o + \delta b \xi, \end{aligned} \quad (2)$$

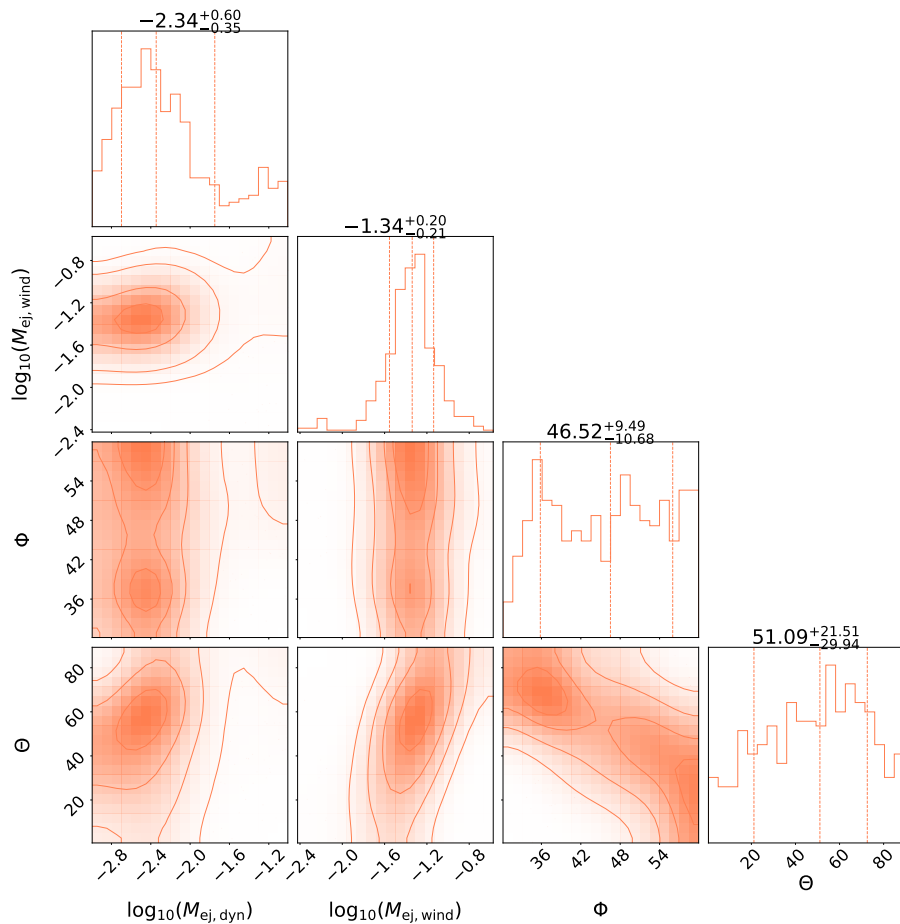


FIG. 7. Estimated ejecta parameters for Model I: the mass of the dynamical ejecta, the mass of the disk wind ejecta, the opening angle between lanthanide-rich and lanthanide-poor dynamical ejecta components, and the viewing angle.

where a_o , b_o , δa and δb are fitting coefficients and ξ is given by

$$\xi = \frac{1}{2} \tanh(\beta(q - q_{\text{trans}})). \quad (3)$$

The right panel of Fig. 10 shows how the fitting changes as the mass ratio change. The plots shows that the updated fit is indeed able to capture the mass ratio dependence.

The best-fit parameters are given by minimizing $r = \langle (\log_{10}(M_{\text{disk}}) - \log_{10}(M_{\text{disk}}^{\text{fit}}))^2 \rangle$: $a_o = -1.581$, $\delta a = -2.439$, $b_o = -0.538$, $\delta b = -0.406$, $c = 0.953$, $d = 0.0417$, $\beta = 3.910$, $q_{\text{trans}} = 0.900$.

Prior combination for distance measurement

Due to the strong correlation between the luminosity distance D and inclination ι_0 inference across different analysis, we combine the information on the D - ι_0 and then marginalize over the inclination. With Bayesian statistics in mind, we take the GRB170817A-VLBI measurement $p_{\text{GRB}}(D, \iota_0)$ as the prior for the other two analysis. Therefore, the combined posterior $p_{\text{com}}(D, \iota_0)$ is given by

$$p_{\text{com}}(D, \iota_0) = \mathcal{L}_{\text{GW}} \times \mathcal{L}_{\text{EM}} \times p_{\text{GRB}}(D, \iota_0), \quad (4)$$

where \mathcal{L}_{GW} and \mathcal{L}_{EM} are the likelihoods for the parameter (D, ι_0) with GW170817 and AT2017gfo analysis, respectively.

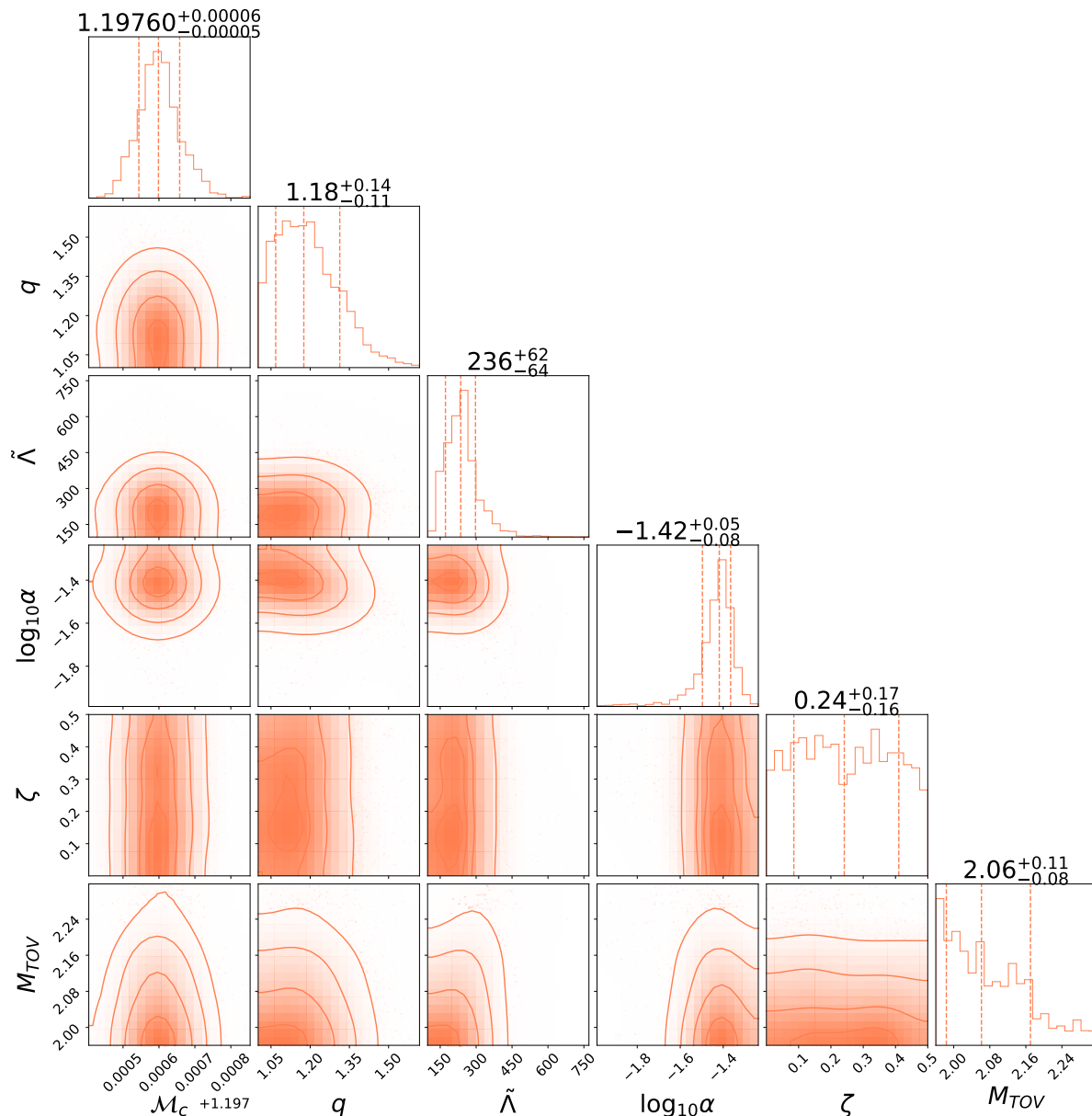


FIG. 8. Estimated parameters for Model I: chirp Mass, mass ratio, tidal deformability, free ejecta parameter α , disk conversion factor ζ , and maximum NS mass. Model II and Model III provide very similar results with respect to the binary properties.

Because we are combining the information in the post-processing stage, we do not have access to the likelihood but the posterior of GW170817 p_{GW} and AT2017gfo p_{EM} only. Therefore, we evaluate the combined posterior by

$$p_{\text{com}}(D, \iota_0) = \frac{p_{\text{GW}}}{\pi_{\text{GW}}} \times \frac{p_{\text{EM}}}{\pi_{\text{EM}}} \times p_{\text{GRB}}(D, \iota_0), \quad (5)$$

where π_{GW} and π_{EM} are the prior for the parameter (D, ι_0) used for analysing GW170817 and AT2017gfo, respectively. The combined posterior on the distance is then given by

$$p_{\text{com}}(D) = \int d\iota_0 p_{\text{com}}(D, \iota_0) \quad (6)$$

which can be later related to the Hubble constant measurement.

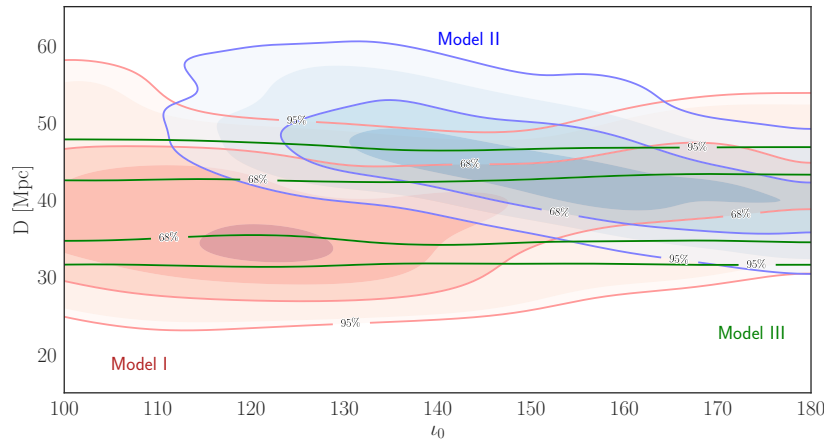


FIG. 9. Distance and inclination measurement for Model I, Model II, and Model III. Model I is the least constraining, but used within the main text since it allows the best physical description of the binary neutron star merger and postmerger phase.

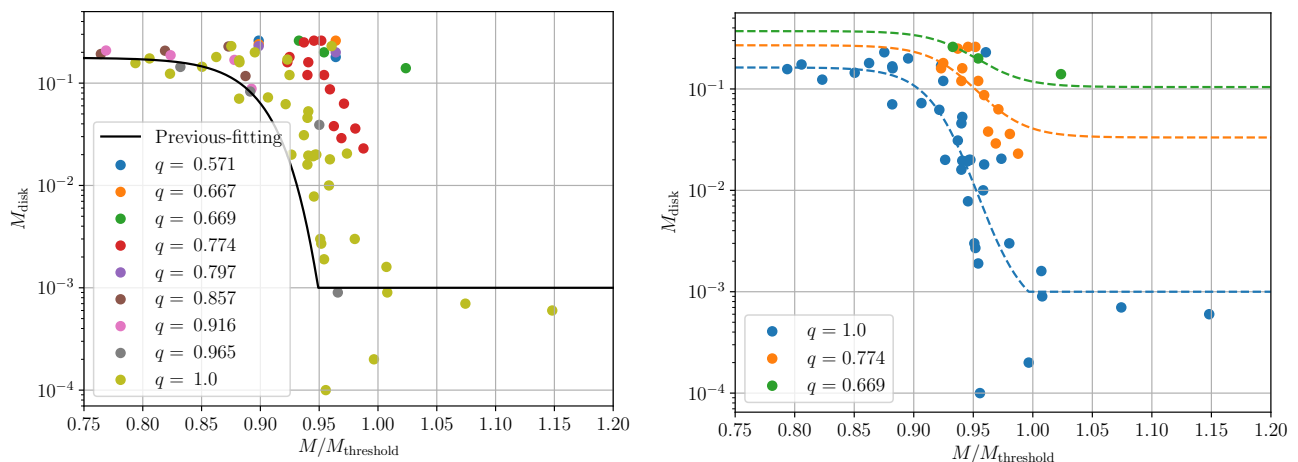


FIG. 10. Left panel: Data employed for the construction of the fit in comparison with the previous fit of [22]. Right panel: A few example cases for different mass ratios with the derived relation on top.

Estimation of the Hubble constant H_0

The Hubble constant H_0 relates the center-of-mass recession velocity relative to the CMB [81] v_r of a galaxy by

$$v_r = H_0 D_c + v_p, \quad (7)$$

where D_c and v_p are the comoving distance and the peculiar velocity, respectively. The distance between the Earth and GW170817 is small (~ 40 Mpc), so that one can approximate the comoving distance with the luminosity distance D .

According to Ref. [82], the collection of galaxies to which GW170817's host galaxy NGC4993 belongs (ESO-508) has a radial velocity of v_r of $3327 \pm 72 \text{ km s}^{-1}$ and according to Ref. [83] the peculiar velocity v_p of NGC4993 is $310 \pm 69 \text{ km s}^{-1}$. In order to reduce the possible systematics introduced by the imperfectly modelling of the bulk flow motion in Ref. [83], we take the uncertainty on the v_p to be 150 km s^{-1} [84].

We model the likelihood of v_r , $\mathcal{L}(v_r)$, and v_p , $\mathcal{L}(v_p)$, to be a Gaussian, which are given by,

$$\mathcal{L}(v_r) \propto \exp\left(-\frac{1}{2} \left(\frac{v_r - \langle v_r \rangle}{\sigma_{v_r}}\right)^2\right), \quad \mathcal{L}(v_p) \propto \exp\left(-\frac{1}{2} \left(\frac{v_p - \langle v_p \rangle}{\sigma_{v_p}}\right)^2\right), \quad (8)$$

where $\langle v_r \rangle = 3327 \text{ km s}^{-1}$, $\sigma_{v_r} = 72 \text{ km s}^{-1}$, $\langle v_p \rangle = 310 \text{ km s}^{-1}$ and $\sigma_{v_p} = 150 \text{ km s}^{-1}$.

As a result, the posterior $p(H_0, D, v_p)$ is given by

$$\begin{aligned}
p(H_0, D, v_p) &= \mathcal{L}(H_0, D, v_p) \pi(H_0, D, v_p) \times \frac{1}{\mathcal{N}_s(H_0)} \\
&\propto \exp\left(-\frac{1}{2} \left(\frac{v_p - \langle v_p \rangle}{\sigma_{v_p}}\right)^2\right) \times \exp\left(-\frac{1}{2} \left(\frac{H_0 D + v_p - \langle v_r \rangle}{\sigma_{v_r}}\right)^2\right) \\
&\times p(D) \times \pi(H_0) \times \pi(v_p) \times \frac{1}{\mathcal{N}_s(H_0)},
\end{aligned} \tag{9}$$

where $p(D)$, $\pi(H_0)$ and $\pi(v_p)$ are the posterior of the distance, the prior on the Hubble constant, and the prior on the peculiar velocity, respectively. And $\mathcal{N}_s(H_0)$ is the selection effect term as described in [4]. We take $\pi(H_0)$ to be uniform in $[20, 160] \text{km s}^{-1} \text{Mpc}^{-1}$, $\pi(v_p)$ to be uniform in $[-c, c]$ and $\mathcal{N}_s(H_0) \propto H_0^3$. [85]

For the posterior of the distance, we take the posterior based on the combined analysis as described above. As we have a set of posterior samples $\{d_i\}$ which follows the posterior $p_{\text{com}}(D)$, we obtain the marginalized posterior $p(H_0, v_p)$ by

$$\begin{aligned}
p(H_0, v_p) &= \int dD p(H_0, D, v_p) \\
&= \int dD p_{\text{com}}(D) \frac{p(H_0, D, v_p)}{p_{\text{com}}(D)} \\
&= \left\langle \frac{p(H_0, D, v_p)}{p_{\text{com}}(D)} \right\rangle_{\{d_i\}},
\end{aligned} \tag{10}$$

in which we approximate $\int dD p_{\text{com}}(D)$ by average over posterior sample $\langle \dots \rangle_{\{d_i\}}$. We sample over the $p(H_0, v_p)$ with emcee [86] and obtain the corner plot shown in Fig. 11.

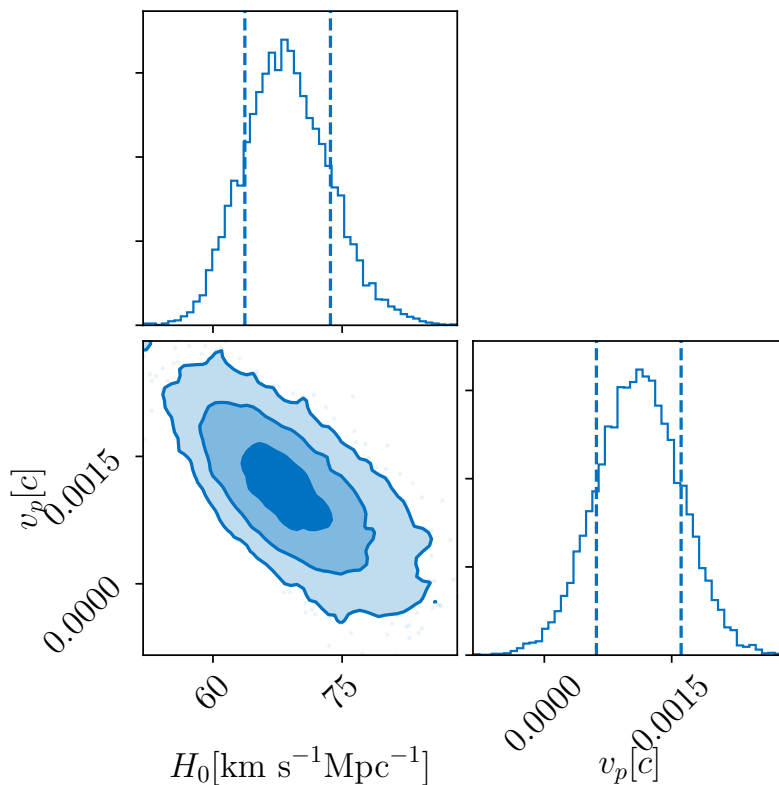


FIG. 11. Corner plot of the inferred H_0 - v_p with the posterior on the distance with combined analysis given.